Applied Physics Letters ARTICLE scitation.org/journal/apl

High-performance dual-gate graphene pH sensors

Cite as: Appl. Phys. Lett. **120**, 263701 (2022); doi: 10.1063/5.0086049
Submitted: 21 January 2022 · Accepted: 10 June 2022 ·
Published Online: 28 June 2022

Son T. Le,[1,a)] Seulki Cho,[1] Alexander Zaslavsky,[1,2] Curt A. Richter,[1] and Arvind K. Balijepalli[1,a)]

AFFILIATIONS

[1]Physical Measurements Laboratory, National Institute of Standards and Technology, Gaithersburg, Maryland 20899, USA
[2]School of Engineering and Department of Physics, Brown University, Providence, Rhode Island 02912, USA

[a)]**Authors to whom correspondence should be addressed:** stle@lps.umd.edu and arvind.balijepalli@nist.gov

ABSTRACT

Field-effect transistors (FETs) are versatile tools for high-precision biophysical measurements, and their measurement sensitivity and resolution can be improved by using innovative materials and device designs. Here, we report on the sensitivity and noise performance of dual-gated graphene FETs. When measuring pH, our devices exhibit a sensitivity of up to 30 V per unit change in pH, ≈500-fold greater than the Nernst value at room temperature, and noise-limited resolution of 2×10^{-4} in the biomedically relevant 0.1–10 Hz bandwidth. This level of performance is obtained due to a highly asymmetric dual-gate design utilizing an ionic liquid top-gate dielectric coupled with graphene's large intrinsic quantum capacitance (≈15 μC/cm^2). Our results improve upon the sensitivity and resolution of previously demonstrated Si- and MoS_2-channel FET biosensors.

Modular field-effect transistor (FET) based measurements, where the signal transduction is separated from the sensing surfaces that interface with biological materials, have been demonstrated for many biotechnology applications, from enzymology to the measurements of protein ligand interactions.[1–6] Importantly, this approach enables measurement platforms that can be adapted rapidly for different applications. The separation of signal transduction from sensing also allows the use of added circuitry to improve sensitivity and resolution, enabling lower limits of detection for the measured analytes. Such setups include closed-loop control and phase sensitive lock-in detection to improve resolution by suppressing noise at the low bandwidths commonly used in biological measurements.[7]

Modular measurement platforms have also allowed the incorporation of innovative FET types. For example, dual-gate devices fabricated from two-dimensional materials, such as MoS_2, have been used within closed-loop control circuitry to achieve record sensitivity and resolution when measuring pH,[2] which can be used as a proxy for enzymatic activity and kinetics.[2–4] The resolution demonstrated by using these approaches exceeds that of both traditional single-gate Si FETs[8–10] and custom-made dual-gate Si FETs[11] by more than two orders of magnitude. In particular, high-resolution measurements can enable numerous applications, such as the quantification of an enzyme function that catalyzes biochemical reactions within cells, improved electronic readout of DNA sequencing approaches that utilize the polymerase chain reaction or isothermal amplification,[9,10,12] and the quantification of electrostatic interactions between macromolecules at extremely low concentrations to complement traditional approaches, such as quartz crystal microbalance[13–15] or surface plasmon resonance.[16–19]

In this Letter, we demonstrate improvements in the sensitivity and resolution of dual-gate devices by using graphene as the FET channel material. Graphene has a theoretically higher quantum capacitance than MoS_2 and is more extensively studied compared to other 2D material technologies. Because wafer-scale growth of high-quality monolayer graphene has been reliably demonstrated,[20] graphene bio-FET sensing can be more mature for large scale applications. Additionally, due to its gapless band structure properties, low-resistance Ohmic contacts to graphene can be produced with a wide range of metals, reducing the requirements for contact engineering. Finally, graphene's high carrier mobility results in high current drive at low source–drain voltages reducing the channel current noise.

In the rest of the paper, we first characterize the electrical performance of ionic-liquid-gated graphene FETs (ILFETs) and then present noise measurements in the constant-current closed-loop mode, to validate the promise of this device structure and demonstrate its advantage over previously reported approaches.

Graphene FETs were fabricated by using a technique we have previously reported in detail.[21–23] Graphene flakes were exfoliated from a highly ordered pyrolytic graphite (HOPG) crystal by using the scotch tape method.[24] The flakes were placed on heavily doped Si substrates covered with ≈285 nm of thermal SiO_2 that also served as a global back-gate. The thickness of the SiO_2 was chosen to provide the optimal optical contrast, making it possible to locate and inspect monolayer graphene flakes with an optical microscope. Subsequently,

electron-beam (e-beam) lithography was used to pattern the source, drain, and gate electrodes followed by e-beam evaporation of metal Ti/Au (nominal 5/100 nm) contacts. After liftoff in acetone and a final resist cleaning by repeated rinsing in acetone, isopropyl alcohol, and de-ionized water, a small droplet of Diethylmethyl(2-methoxyethyl)ammoniumbis(trifluoromethylsulfonyl)imide (DEME-TFSI) IL was applied to each device by using a micromanipulator under an optical microscope. Importantly, ILs were used as the gate dielectric due to their extremely small equivalent oxide thickness (EOT) of <1 nm, which provided strong coupling between the gate and the graphene channel. The droplet was sized to cover the monolayer graphene and the gate electrodes. The device schematic is shown in Fig. 1(a), whereas an optical image of the final device is shown in Fig. 1(b). It is important to note that for good ionic liquid-gate coupling with the graphene channel, the area of the gate electrode that is in contact with the ionic liquid was designed to be much larger than the combined area of the source and drain contacts together with the graphene channel itself.

Following the IL gate deposition, the devices were loaded into a high-vacuum chamber probe station and pumped for more than 24 h to a final pressure of $\approx 13 \times 10^{-6}$ Pa (10^{-7} Torr) to completely desorb moisture from the ionic liquid. Electrical characterization and remote pH sensing measurements using these dual-gated graphene devices were performed while the devices were kept under high vacuum. Device stability and performance were not observed to degrade over several months under vacuum.

The transfer characteristics of our graphene FETs were measured by recording the drain current (I_D) as a function of the top liquid-gate potential (V_{LG}) with the drain voltage (V_D) held constant (all voltages referenced to the grounded source of the FET).[2,25] The measurements were repeated for different back-gate voltages (V_{BG}) to determine the signal amplification (α) due to the asymmetric capacitance of the top and back gates.[2] Figure 2(a) shows the transfer characteristics of a representative device showing the source-drain resistance as a function of V_{LG} with $V_D = 5$ mV and V_{BG} stepped from −20 to 40 V in 5 V steps. The Dirac point voltage (V_{Dirac}), defined as the top-gate V_{LG} voltage at which channel resistance reaches its maximum, is ≈0 V, indicating

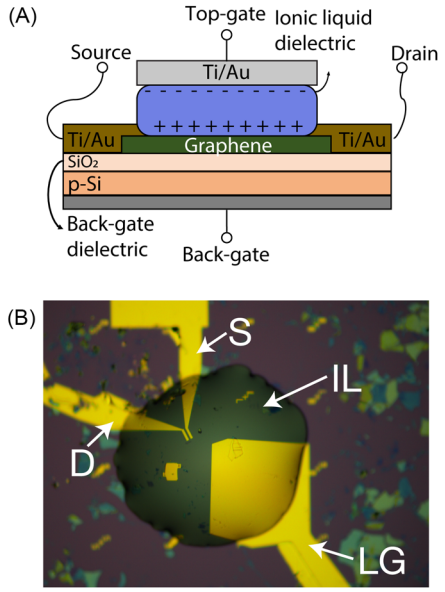

FIG. 1. (a) Schematic representation of the ionic liquid-gate graphene field-effect transistor (FET). (b) Representative graphene ILFET device comprised of source (S), drain (D), and liquid-gate (LG) terminals.

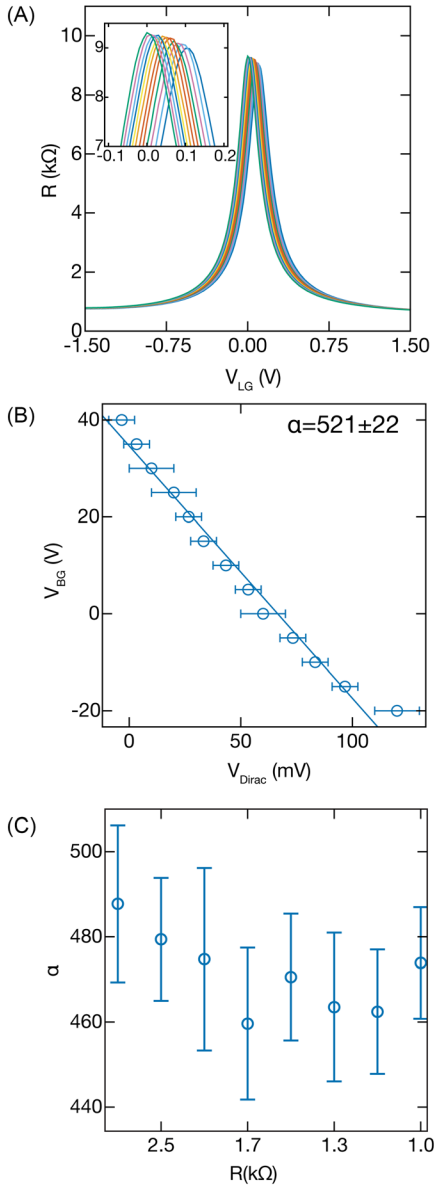

FIG. 2. (a) Transfer characteristics of an ionic liquid-gate graphene field-effect transistor (FET) as a function of back-gate voltage V_{BG} in the −20 to 40 V range. Inset shows close-up of the resistance maximum Dirac point V_{Dirac}. (b) V_{BG} as a function of the shift in V_{Dirac}, slope represents the device gain α. The error bars represent the standard deviation of three independent measurements, while the error in the fit parameter is the standard error with expanded uncertainty $k = 2$. (c) Gain α as a function of the channel resistance R. The error bars represent the standard error in the fit parameter α ($k = 2$).

low residual surface contamination from the fabrication steps. Moreover, the resistance at the Dirac point is ≈9 kΩ, more than an order of magnitude higher than that at $|V_{LG}| > 1$ V. These properties are indicative of high-quality graphene and of good Ohmic contacts with a contact resistance on the order of a few hundred Ohms. As a result, we performed all our measurements at $V_D = 2$–5 mV (I_D between 1 and 5 μA). The high current values at low V_D enabled accurate current and noise measurements while avoiding Joule self-heating.

In Fig. 2(a), V_{Dirac} was determined for each curve as the value of V_{LG} associated with the maximum channel resistance. [The inset in Fig. 2(a) shows a detailed view of the transfer curves around the Dirac point.] In Fig. 2(b), we plot the V_{BG} for each curve in Fig. 2(a) as a function of V_{Dirac}. The gain in the device is $\alpha \equiv dV_{BG}/dV_{LG}$ at a constant I_D that was determined numerically. We found α to have a large and approximately constant value of 521 ± 22 (where the error bar is the standard error in the fit parameter of the weighted linear regression in Fig. 2(b) with expanded uncertainty; $k = 2$). Such a high gain is possible due to the high intrinsic quantum capacitance of graphene and its strong capacitive coupling with the ionic liquid. The total top gate capacitance C_{TG} arises from the liquid-gate capacitance C_{LG} in series with the quantum capacitance of graphene C_{QG}: $C_{TG} = C_{QG}C_{LG}/(C_{QG} + C_{LG})$. Similarly, for the back gate capacitance C_{BG}, we have $C_{BG} = C_{QG}C_{OX}/(C_{QG} + C_{OX}) \approx C_{OX}$, where C_{OX} is the back gate oxide capacitance. In particular, the 285 nm SiO_2 oxide thickness used in this study results in $C_{OX} = 0.0124$ μF/cm^2, which is considerably smaller than C_{QG} and $C_{LG} = 10.7$ μF/cm^2.[2] Using the equations above, we estimate the resulting quantum capacitance of the graphene channel $C_{QG} \approx 16.3$ μF/cm^2 at the Dirac point. This value is about a factor of 2 higher than previously reported measurements for ionic-liquid-gated graphene,[26] possibly due to higher impurity interface charge density at the graphene–liquid interface in those studies. Importantly, the graphene quantum capacitance is roughly ≈7.5 times larger than that of 2D-MoS_2,[2,27] resulting in improved gain in graphene-based devices compared to MoS_2 ILFETs.

Estimating the gain at the Dirac point is useful for benchmarking the maximum possible α. On the other hand, optimal pH measurements using constant-current closed-loop techniques (described next) require finding α at predetermined values of I_D away from the Dirac point. In Fig. 2(c), we present the values of α extracted from the V_{LG} vs V_{BG} dependence of I_D at fixed values between 1 and 5 μA. [The V_{LG} range used for Fig. 2(c) was between −0.4 and −0.1 V, to the left of the Dirac point in Fig. 2(a).]. We observe that α remains high and constant over this range of I_D, enabling the high-precision constant-current measurements described in the next paragraph.

After the graphene devices were parametrically characterized, we embedded them within the circuitry shown schematically in Fig. 3(a) to realize a biosensing system. Our approach, which operates the dual-gate devices within a closed-loop control system[3,4] and utilizes lock-in detection, allows us to perform time-resolved measurements with high sensitivity, while also greatly improving noise performance between 0.1 and 10 Hz: a bandwidth that is relevant to biological applications that we target with this approach. The principles for applying closed-loop control with dual-gate devices have been described previously.[2] Briefly, we maintain the channel current I_D at a constant value by continually adjusting V_{BG} with a proportional-integral-derivative (PID) controller in response to a voltage change to the ionic liquid V_{LG} top gate that responds to changes in the pH of the solution being measured

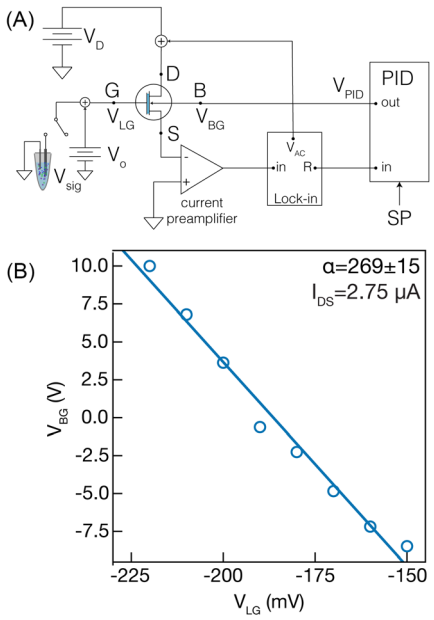

FIG. 3. (a) Schematic representation of the circuit used for constant current measurements with dual-gate graphene ILFETs. (b) Back-gate voltage V_{BG} as a function of the ionic liquid-gate voltage V_{LG} used to determine the gain α at constant $I_D = 2.75$ μA. The standard deviation of V_{BG} at each value of V_{LG} was smaller than the symbols in the plot. The uncertainty in α represents the standard error in the fit parameter α with expanded uncertainty, $k = 2$.

by the sensing electrode. The small changes in V_{LG} are amplified by the gain α. An offset voltage, V_O, is summed with the sensor voltage to bias the graphene channel to the desired I_D value along the transfer curve [Fig. 2(a)]. Figure 3(b) plots the V_{BG} as a function of the V_{LG} in the PID mode with constant $I_D = 2.75$ μA. The value of $\alpha = dV_{BG}/dV_{LG}$ was extracted at $I_D = 2.75$ μA from a linear fit of the data and found to be 269 ± 15. This value was ≈4 times larger than that of the 2D-MoS_2 ILFET under a similar measurement configuration.[2]

To further improve the noise performance of our measurements, we integrated a lock-in amplifier into our sensing system.[4] A small AC signal ($f = 100$ kHz) was added to the DC drain voltage V_D applied to the channel. The drain current was amplified with a high-bandwidth current pre-amplifier, and the AC component of the current was then demodulated with the lock-in amplifier. The output of the lock-in amplifier was first filtered by using a fourth order lowpass Bessel filter with a cutoff frequency of 5 kHz and then connected to the PID controller. The narrowband detection enabled by the lock-in amplifier can provide added noise suppression, depending on the main sources of noise in the system. Below, we will show that our graphene ILFETs can provide record resolution and signal-to-noise ratio when integrated within the combined measurement circuitry.

We investigated the sources of noise and their impact on the resolution of the graphene ILFETs in constant current mode. Two measurement configurations were tested to identify noise sources that could limit performance. The first was a low-noise voltage source that provided a DC potential to the ionic liquid-gate of the device, and the second was a pH sensing electrode in contact with buffered electrolyte solution that could potentially introduce additional noise. The same

graphene ILFET was used to measure buffered solutions corresponding to pH 4–pH 10.

A comparison of the power spectral density (PSD) of the V_{BG} noise up to $f = 50$ Hz between both types of measurements is presented in Fig. 4, with each configuration schematically depicted in the inset. In Fig. 4(a), the $V_{LG} = V_O = -237$ mV was set with a voltage source, whereas in Fig. 4(b), V_{LG} was set by summing $V_O = -50$ mV with the signal provided by a microelectrode immersed in a pH = 4 solution. The PSD results in Figs. 4(a) and 4(b) are indistinguishable (and the same was true for other pH values in the measured 4–10 range, compared to a voltage source). Furthermore, the root-mean-squared (RMS) noise in V_{BG}, given by $[\int S_{VBG}\, df]^{1/2}$ integrated from 0.1 to 10 Hz, was found to be 5.5 and 5.6 mV for the constant voltage source and pH sensor summed with a constant voltage, respectively. This indicates that the added noise due to the pH sensor itself is negligible and that the RMS noise in the system is limited by the graphene ILFET and the measurement electronics.

The excellent noise characteristics of the graphene ILFET were then combined with the closed-loop constant-current approach described above. The PSD of the graphene channel drain current noise S_{ID} is illustrated in Fig. 5 for a series of input signals V_{LG} ranging from −150 to −220 mV. When operated in an open-loop, as in Fig. 5(a), we observe $1/f$ noise commonly reported in the literature for FET-based sensors.[11,28–30] Conversely, under closed-loop operation with PID

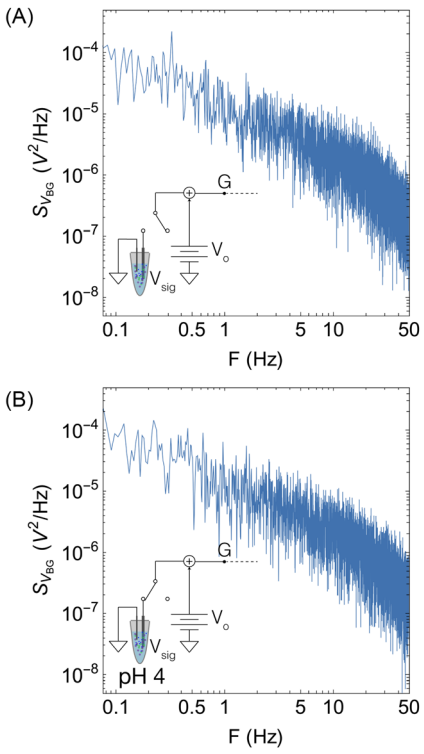

FIG. 4. (a) Power spectral density (PSD) of the back-gate voltage when connected to a constant voltage source V_O. (b) PSD of the back-gate voltage when connected to a pH sensor immersed in a pH = 4 solution summed with a constant voltage. Insets show schematically the V_{LG} input signal for the data in each panel.

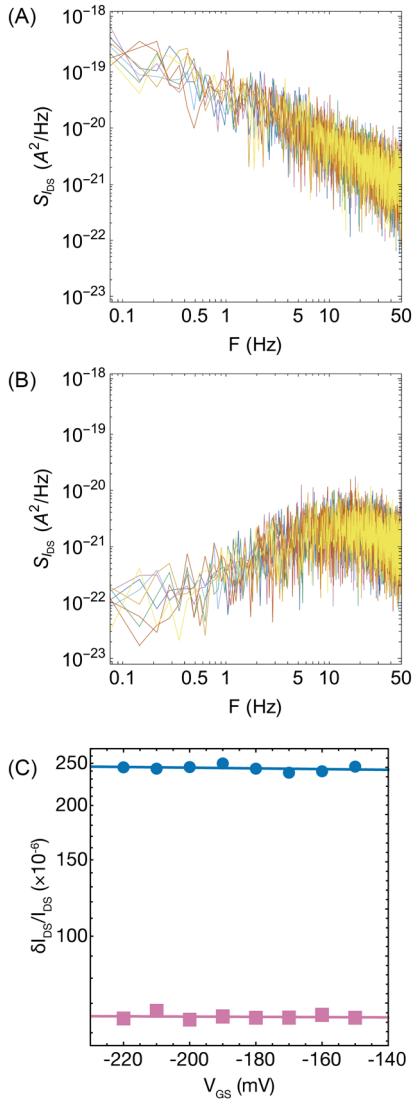

FIG. 5. (A) Power spectral density (PSD) of the channel current I_D when the graphene ILFET was operated in open-loop mode vs V_{LG}. (B) PSD of I_D when the graphene ILFET was operated under closed-loop control vs V_{LG}. (C) Comparison of the broadband root-mean-squared (RMS) noise in the 0.1–10 Hz frequency range as a function of V_{LG} for open-loop (blue) and closed-loop (pink) operation.

control, as in Fig. 5(b), the noise in the biologically relevant 0.1–10 Hz frequency range is strongly suppressed. The noise suppression due to PID control can be quantified by the channel current RMS noise δI_D obtained by integrating S_{ID} over the 0.1–10 Hz bandwidth and taking the square root, $\delta I_D = [\int S_{ID}\, df]^{1/2}$. The current noise results scaled by the magnitude of I_D, $\delta I_D/I_D$, are summarized for the entire range of V_{LG} in Fig. 5(c). We observe that PID control improves the relative current noise by a factor of ≈4. Quantifying the noise suppression using the PID approach will be the subject of further studies. Interestingly, the scaled RMS noise is independent of I_D (and thereby V_{LG} or, equivalently, the actual pH value of the solution), making it

possible to perform measurements with high dynamic range without compromising the noise characteristics.

Our approach to quantitatively measure the pH sensitivity and resolution has been described previously.[2] Briefly, a histogram from the raw V_{PID} time-series data was computed for each measured pH. A sum of two Gaussian distribution functions was then fit to the histograms to obtain the peak positions and standard deviations of the reference potential and the measured pH signal. The difference in the peak positions between the pH and reference potentials (ΔV_{PID}) was used to determine the pH sensitivity. The measurement uncertainty σ_{PID} was then obtained by propagating the error when determining ΔV_{PID}. For the graphene ILFETs, we set $\Delta pH = (k \times \sigma_{PID})/(\alpha \times V_{Nernst})$, where $k = 2$ is the expanded uncertainty and $V_{Nernst} \approx 59$ mV at room temperature. Three graphene ILFETs were tested, with similar but not identical performance; the same device presented in Figs. 1–5 was used to estimate the pH resolution. Measurements were performed by washing the sensors between subsequent pH solutions. The equilibration time was fast with the sensors reaching a steady-state value in under 10 s.

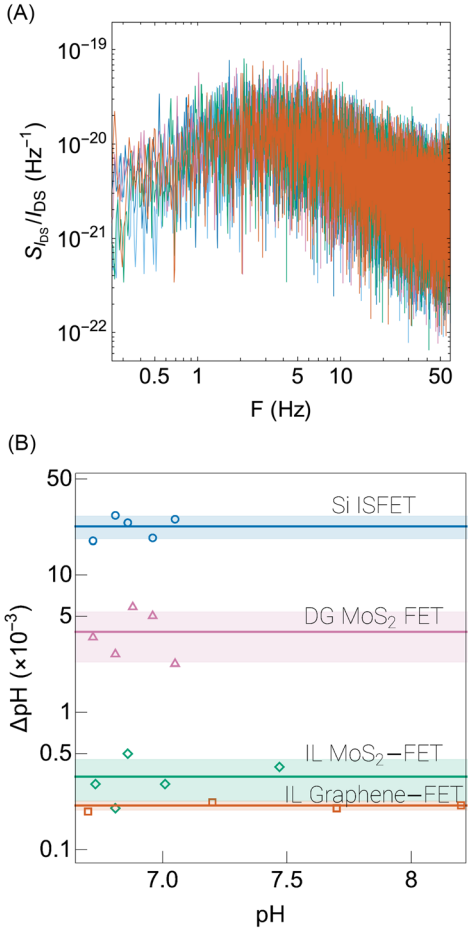

FIG. 6. (A) Power spectral density (PSD) of the channel current I_D when the graphene ILFET was operated in a closed-loop mode. The ionic liquid-gate was connected to a pH sensor immersed in pH solutions shown in panel B. (B) Comparison of FET-based pH sensor resolution across physiologically relevant pH values. The solid lines indicate the mean pH resolution for each sensor, while the colored bands show the standard deviation with expanded uncertainty ($k = 2$).

Figure 6(a) shows the PSD of I_D when a pH sensor, connected to the ionic liquid-gate, is immersed in electrolyte solutions with pH adjusted between 6.2 and 8.5. The PSD, shown over the relevant bandwidth range of 0.1–60 Hz, is virtually identical, indicating that the noise in the measurements is dominated by the ILFET and not the pH sensor. The data in the PSD in Fig. 6(a) were integrated and converted to pH resolution in Fig. 6(b). The results compare our graphene ILFETs with FET-based pH measurements previously reported in the literature.[2–4] Graphene FETs show a marked resolution advantage over single-gated Si FETs and dual-gated solid-state MoS_2 2D-FETs. The improvement in pH resolution is ≈2 orders of magnitude over single-gated Si FETs and ≈1 order of magnitude over the dual-gated solid-state MoS_2 FETs, showing the benefit of the strong capacitive coupling between the graphene channel and the ionic liquid. Compared to ionic-liquid dual-gated MoS_2 2D-FETs, the improvement in resolution of graphene ILFETs reported here is modest [$(0.21 \pm 0.02) \times 10^{-3}$ vs $(0.34 \pm 0.1) \times 10^{-3}$] as seen from Fig. 6. Still, the resolution values for graphene ILFETs at different pH values have a lower uncertainty in comparison with that of dual-gated MoS_2 ILFETs over the full range of pH values, suggesting that graphene FETs have more stable operating characteristics. Combined with better large area growth, ease of fabrication, and better performance, graphene FET-based pH measurement systems show the potential for widespread adoption in the biochemical measurement community.

In conclusion, we demonstrate that FET-based modular measurements can benefit from dual-gate device designs and from the high intrinsic quantum capacitance of graphene. These properties allow measurements with a high intrinsic device gain, enabling measurements of pH with a sensitivity ≈500-fold greater than the Nernst value at room temperature. They also resulted in a noise-limited pH resolution of 2×10^{-4} in the biologically relevant 1–10 Hz bandwidth. The results represent a ≈20-fold improvement in resolution compared with traditional silicon ISFETs and a 50% improvement over dual-gate MoS_2 FETs. The lower uncertainty of the graphene FETs and improved manufacturability can allow them to be applied to numerous applications in biotechnology and biophysics.

S.T.L. acknowledges support by the National Institute of Standards and Technology (NIST, Grant No. 70NANB16H170). A.Z. acknowledges sabbatical support through the Brown/NIST PREP program (NIST, Grant No. N70NANB18H160). This research was performed, in part, at the NIST Center for Nanoscale Science and Technology nanofabrication facility.

AUTHOR DECLARATIONS

Conflict of Interest

The authors have no conflicts to disclose.

Author Contributions

Son T. Le: Conceptualization (equal); Data curation (equal); Formal analysis (equal); Investigation (equal); Methodology (equal); Validation (equal); Visualization (equal); Writing – original draft (equal); Writing – review and editing (equal). **Seulki Cho:** Data curation (equal); Writing – review and editing (equal).

Alexander Zaslavsky: Data curation (equal); Formal analysis (equal); Writing – original draft (equal); Writing – review and editing (equal). **Curt A. Richter:** Funding acquisition (equal); Project administration (equal); Supervision (equal); Writing – original draft (equal); Writing – review and editing (equal). **Arvind K. Balijepalli:** Conceptualization (equal); Data curation (equal); Investigation (equal); Project administration (equal); Writing – original draft (equal); Writing – review and editing (equal).

DATA AVAILABILITY

The data that support the findings of this study are available from the corresponding author upon reasonable request.

REFERENCES

[1]A. Tarasov, M.-Y. Tsai, E. M. Flynn, C. A. Joiner, R. C. Taylor, and E. M. Vogel, 2D Mater. **2**, 044008 (2015).
[2]S. T. Le, N. B. Guros, R. C. Bruce, A. Cardone, N. D. Amin, S. Zhang, J. B. Klauda, H. C. Pant, C. A. Richter, and A. Balijepalli, Nanoscale **11**, 15622–15632 (2019).
[3]S. T. Le, M. A. Morris, A. Cardone, N. B. Guros, J. B. Klauda, B. A. Sperling, C. A. Richter, H. C. Pant, and A. Balijepalli, Analyst **145**, 2925–2936 (2020).
[4]S. T. Le, S. Cho, C. A. Richter, and A. Balijepalli, Rev. Sci. Instrum. **92**, 030901 (2021).
[5]H.-J. Jang, T. Lee, J. Song, L. Russell, H. Li, J. Dailey, P. C. Searson, and H. E. Katz, ACS Appl. Mater. Interfaces **10**, 16233–16237 (2018).
[6]H.-J. Jang, J. Wagner, H. Li, Q. Zhang, T. Mukhopadhyaya, and H. E. Katz, J. Am. Chem. Soc. **141**, 4861–4869 (2019).
[7]A. Susloparova, D. Koppenhöfer, X. T. Vu, M. Weil, and S. Ingebrandt, Biosens. Bioelectron. **40**, 50–56 (2013).
[8]K. McLaughlin, A. Dickson, S. B. Weisberg, K. Coale, V. Elrod, C. Hunter, K. S. Johnson, S. Kram, R. Kudela, T. Martz, K. Negrey, U. Passow, F. Shaughnessy, J. E. Smith, D. Tadesse, L. Washburn, and K. R. Weis, Reg. Stud. Mar. Sci. **12**, 11–18 (2017).
[9]C. Toumazou, L. M. Shepherd, S. C. Reed, G. I. Chen, A. Patel, D. M. Garner, C.-J. A. Wang, C.-P. Ou, K. Amin-Desai, P. Athanasiou, H. Bai, I. M. Q. Brizido, B. Caldwell, D. Coomber-Alford, P. Georgiou, K. S. Jordan, J. C. Joyce, M. L. Mura, D. Morley, S. Sathyavruthan, S. Temelso, R. E. Thomas, and L. Zhang, Nat. Methods **10**, 641–646 (2013).
[10]J. M. Rothberg, W. Hinz, T. M. Rearick, J. Schultz, W. Mileski, M. Davey, J. H. Leamon, K. Johnson, M. J. Milgrew, M. Edwards, J. Hoon, J. F. Simons, D. Marran, J. W. Myers, J. F. Davidson, A. Branting, J. R. Nobile, B. P. Puc, D. Light, T. A. Clark, M. Huber, J. T. Branciforte, I. B. Stoner, S. E. Cawley, M. Lyons, Y. Fu, N. Homer, M. Sedova, X. Miao, B. Reed, J. Sabina, E. Feierstein, M. Schorn, M. Alanjary, E. Dimalanta, D. Dressman, R. Kasinskas, T. Sokolsky, J. A. Fidanza, E. Namsaraev, K. J. McKernan, A. Williams, G. T. Roth, and J. Bustillo, Nature **475**, 348–352 (2011).
[11]T. Wu, A. Alharbi, K.-D. You, K. Kisslinger, E. A. Stach, and D. Shahrjerdi, ACS Nano **11**, 7142–7147 (2017).
[12]D. Ma, J. Rodriguez-Manzano, S. de Mateo Lopez, M. Kalofonou, P. Georgiou, and C. Toumazou, IEEE Trans. Biomed. Circ. Syst. **12**, 1186–1201 (2018).
[13]N. Atar and M. L. Yola, Anal. Chim. Acta **1148**, 338202 (2021).
[14]J. Zhang, X. Zhang, X. Wei, Y. Xue, H. Wan, and P. Wang, Anal. Chim. Acta **1164**, 338321 (2021).
[15]R.-Z. Hao, H.-B. Song, G.-M. Zuo, R.-F. Yang, H.-P. Wei, D.-B. Wang, Z.-Q. Cui, Z. Zhang, Z.-X. Cheng, and X.-E. Zhang, Biosens. Bioelectron. **26**, 3398–3404 (2011).
[16]D. Daems, W. Pfeifer, I. Rutten, B. Saccà, D. Spasic, and J. Lammertyn, ACS Appl. Mater. Interfaces **10**, 23539–23547 (2018).
[17]S. G. Patching, Biochim. Biophys. Acta **1838**, 43–55 (2014).
[18]X. Shan, U. Patel, S. Wang, R. Iglesias, and N. Tao, Science **327**, 1363–1366 (2010).
[19]K. A. Willets and R. P. Van-Duyne, Annu. Rev. Phys. Chem. **58**, 267–297 (2007).
[20]J.-H. Lee, E. K. Lee, W.-J. Joo, Y. Jang, B.-S. Kim, J. Y. Lim, S.-H. Choi, S. J. Ahn, J. R. Ahn, M.-H. Park, C.-W. Yang, B. L. Choi, S.-W. Hwang, and D. Whang, Science **344**, 286–289 (2014).
[21]N. N. Klimov, S. T. Le, J. Yan, P. Agnihotri, E. Comfort, J. U. Lee, D. B. Newell, and C. A. Richter, Phys. Rev. B **92**, 241301 (2015).
[22]X. Liang, B. A. Sperling, I. Calizo, G. Cheng, C. A. Hacker, Q. Zhang, Y. Obeng, K. Yan, H. Peng, Q. Li, X. Zhu, H. Yuan, A. R. H. Walker, Z. Liu, L. Peng, and C. A. Richter, ACS Nano **5**, 9144–9153 (2011).
[23]S. T. Le, A. F. Rigosi, J. A. Hagmann, C. Gutiérrez, J. U. Lee, and C. A. Richter, Phys. Rev. B **105**, 045407 (2022).
[24]K. S. Novoselov, A. K. Geim, S. V. Morozov, D. Jiang, Y. Zhang, S. V. Dubonos, I. V. Grigorieva, and A. A. Firsov, Science **306**, 666–669 (2004).
[25]N. B. Guros, S. T. Le, S. Zhang, B. A. Sperling, J. B. Klauda, C. A. Richter, and A. Balijepalli, ACS Appl. Mater. Interfaces **11**, 16683–16692 (2019).
[26]J. Xia, F. Chen, J. Li, and N. Tao, Nat. Nanotechnol. **4**, 505–509 (2009).
[27]N. Ma and D. Jena, 2D Mater. **2**, 015003 (2015).
[28]S. Zafar, C. D'Emic, A. Jagtiani, E. Kratschmer, X. Miao, Y. Zhu, R. Mo, N. Sosa, H. Hamann, G. Shahidi, and H. Riel, ACS Nano **12**, 6577–6587 (2018).
[29]A. Tarasov, W. Fu, O. Knopfmacher, J. Brunner, M. Calame, and C. Schönenberger, Appl. Phys. Lett. **98**, 012114 (2011).
[30]J. Go, P. R. Nair, and M. A. Alam, J. Appl. Phys. **112**, 34516 (2012).